

Thermotropic Vine-inspired Robots

Shivani Deglurkar^{1*}, Charles Xiao^{1*}, Luke Gockowski¹, Megan T. Valentine¹, and Elliot W. Hawkes¹

Abstract—Soft and bio-inspired robotics promise to imbue robots with capabilities found in the natural world. However, many of these biological capabilities are yet to be realized. For example, current vine- and root-inspired everting robots rely on centralized control outside of the robotic tendril to process sensor information and command actuation. In contrast, roots in nature control growth direction in a distributed manner, with all control, sensing, and actuation local. Such distributed control is useful for robustness and parallelization particularly while the plants search for resources (light, water, favorable soil, etc.). Here we present an approach for exploiting these biological behaviors via a thermotropic vine-inspired robot; the device uses local, material-level sensing, actuation, and control embedded in its skin to grow toward a source of heat. We present basic modeling of the concept, design details, and experimental results showing its behavior in varied heat fields. Our simple device advances vine-inspired everting robots by offering a new, distributed method of shape control, and could lead to eventual applications such as highly parallelized robots for fire-fighting or search-and-rescue operations.

I. INTRODUCTION

Over the past decades, bio-inspired robotics and then soft robotics have gained interest [1], owing partly to their ability to easily adapt to changing environments without complex mechanisms. Vine-inspired everting robots, or “vine robots,” are a class of soft robot made of an inverted, flexible, thin-walled pneumatic tube that everts when pressurized, lengthening from its tip [2], [3], [4], [5], [6], [7]. Because this lengthening involves no relative movement of the body with respect to the environment, the robot can reliably extend through constrained environments, even when the properties of the path and obstacles are unknown.

Current control schemes for vine robots are centralized, relying on sensor data processed by either human operators or an autonomous computer controller to steer towards a target. For human-controlled teleoperation, the operator receives information from the sensors, decides on the control scheme, and sends the appropriate signal(s) to the robot (e.g., [8]). For autonomous control, computer vision can be implemented to parse a scene and direct the robot to a pre-determined target (e.g., [7]). Another method of centralized control scheme uses tropisms, or directed motility along a gradient [9]. Tropisms have been demonstrated in a plant-inspired robot with embedded sensing capabilities and a sensorized root-inspired centralized control algorithm [10].

This work was supported in part by NSF Grants CMMI-1944816 and EFMA-1935327. The work of C. Xiao was supported by the NSF Graduate Research Fellowship Program.

¹Department of Mechanical Engineering, University of California, Santa Barbara, CA 93106.

* Equal contribution. Emails: shivani_deglurkar@ucsb.edu, charles_xiao@ucsb.edu

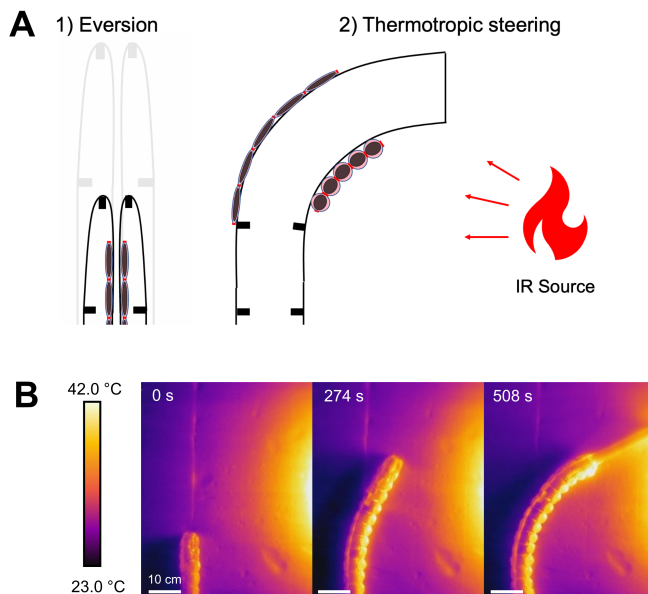


Fig. 1. **A:** Schematic of thermotropic vine-inspired robot concept. **B:** Realization of the concept: a pneumatic everting robot grows forward and toward the right where the heat source is located. Image taken with an IR camera.

While such centralized control is useful when a single robot is employed, it has limitations when many robots are needed, for example, to run a large-scale parallelized search of a space. A human operator simply cannot control dozens of robots simultaneously, and a centralized autonomous system grows unfeasibly complex (wiring, valving and pumps for actuators, etc.) and increasingly expensive as the central base of the robot controls a larger and larger number of “tendrils.”

Distributed control [11] is a different paradigm that has the potential to address these challenges, and a version of it is found in biological vines and roots [12]. In these natural systems, growth is directed by environmental cues sensed by each individual vine or root without any central processing. For root systems, hundreds or even thousands of individual roots can simultaneously steer. Further, if some of the vines or roots are damaged or removed, the others remain fully functional. In robotics, swarms and collectives demonstrate effective use of distributed control (e.g., [13], [14], [15]).

In practical terms, implementation of such a distributed control scheme in a robot containing many vine-like tendrils, requires that the sensing-control-actuation system found in each tendril is simple and inexpensive. Current steering mechanisms for vine robots, including motorized pull tendons (e.g., [16]), pneumatically-controlled latches (e.g., [7]), and artificial muscles (e.g., [8], [17], [18]), all require electronic

sensing, control, and power, limiting their use in highly parallelized distributed control systems. A promising alternative is a “material-level” scheme that leverages the intrinsic materials properties of the soft robot body. The capabilities of a number of functional materials to sense, compute, or actuate in response to external stimuli (such as heat, light, electromagnetic fields, or chemical conditions) have been demonstrated [19], [20]. Among these, thermal stimuli are particularly promising due to the availability of phase change materials that can undergo significant changes in properties or volume as a function of temperature [21], [22].

In this work, we present a decentralized control method for vine-like robots that uses material-level sensing-control-actuation loops embedded directly in the skin to achieve thermotropism—i.e., directed motion toward a heat source (Figure 1). The local sensing and actuation is achieved using the liquid-gas phase change of a low-boiling-point fluid that is distributed along the sides of an everting robot body using series pneumatic artificial muscles (sPAMs) [23]. The sPAMs located on the robot side closest to the heat source will actuate first, shortening that side of the robot, and steering it toward the heat source. In this way, we develop the first everting robot with distributed, material-level control.

What follows is a description of the design and fabrication of the device, a model describing the coupled mechanical and heat transfer effects present in heat-activated artificial muscles, experimental characterization of sPAM actuation and the demonstration of a heat-activated vine robot extending towards a heat source. We conclude with a discussion of the robot performance and next steps.

II. DEVICE DESIGN

A. Heat-activated sPAM Design

The basic concept for the actuator is based on the pleated pneumatic artificial muscle [24], [25], which when arranged in series, form a sPAM [23]. Increasing internal pressure results in volumetric expansion, radial swelling, and length contraction. Such actuators have been traditionally actuated by pumping compressed fluid into the device using a continuous fluid passageway, such that a single source of pressurized air causes all pouches to inflate. This limits the possibility of local curvature control. In contrast, we isolate the inflation of each segment in the series by sealing it individually, thereby enabling localized actuator response. Further, instead of using a pneumatic pump, we fill the actuator with a low-boiling-point fluid that vaporizes when heated, causing a local increase in pressure and enabling local curvature control. We select Novec 7000 as a working fluid due to its low boiling point (i.e., 34 °C at atmospheric pressure), non-toxicity, and compatibility with a broad selection of polymer films. We use a quartz heater (Infratech W-7512 SS) with an approximate emission peak of 3.2 μm , although the presented design process could be adapted for other heat sources, such as fire.

Choosing an appropriate IR absorber and designing its placement is critical to creating a fast thermotropic actuator response. We considered two paradigms: either using an opaque,

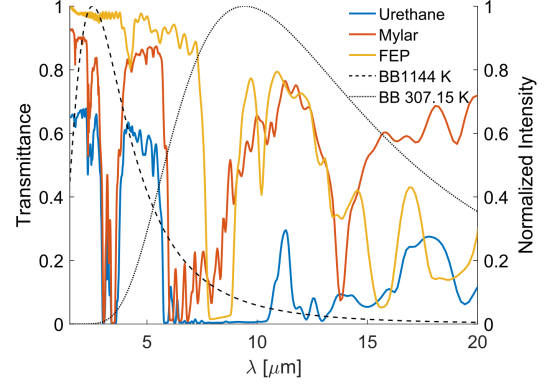


Fig. 2. Transmittance measurements of different materials polymeric materials (solid lines, left axis). The normalized intensity of the blackbody radiation representing the heater (dotted line, right axis) and an object held at the boiling point of Novec 7000 (dashed line, right axis).

absorbing material for the sPAM skin, which requires heat to be conducted to the contained fluid, or using an IR-transparent pouch with an IR-absorber immersed in the working fluid. In the latter case, the skin should be transparent to the primary wavelengths of the heat source and opaque to the emissive wavelengths of the robot’s operating temperature, to create a greenhouse effect [26].

To select an appropriate IR-transparent plastic film, we compared the transmittance of urethane, Mylar, and fluorinated ethylene propylene (FEP) films (Figure 2) to the estimated blackbody spectrum of our heater, as well as the black body spectrum of an object at 307.15 K, which is the boiling point of Novec 7000. Both the Mylar and FEP films show good transmittance to the heat source wavelengths; however, Mylar has the best durability and lowest gas permeability of the films tested and thus was used throughout.

To test the effect of absorber configuration on response time, we measured the time for a single pouch to transition from fully deflated to fully inflated when fixed to a polystyrene foam block positioned 76 cm away from the quartz heater. Each pouch (7.0 cm \times 3.7 cm) was heat sealed with equal volumes of Novec 7000 inside. Four conditions were tested: (A) clear Mylar pouch containing a black nonwoven microfiber sheet (EonTex NW170-PI-20), (B) clear Mylar pouch with the microfiber sheet adhered to the surface using double-sided tape, (C) aluminized Mylar pouch with a microfiber sheet adhered to its surface, (D) aluminized Mylar pouch with the surface coated with matte black spraypaint (Krylon Ultra Flat Camouflage). The response times of A, B, C, and D were 95, 270, 105, and 150 seconds, respectively. The fastest configuration, clear Mylar containing an internal microfiber sheet, was selected for robot fabrication.

B. Robot Design

The robot is composed of a central spine comprised of a pneumatically pressurized LDPE tube (lay-flat width, 5 cm) that provides for overall growth, flanked by two Novec 7000 filled sPAMs (Figure 1). The sPAMs are small and supple for eversion. Left-right steering is achieved by differential

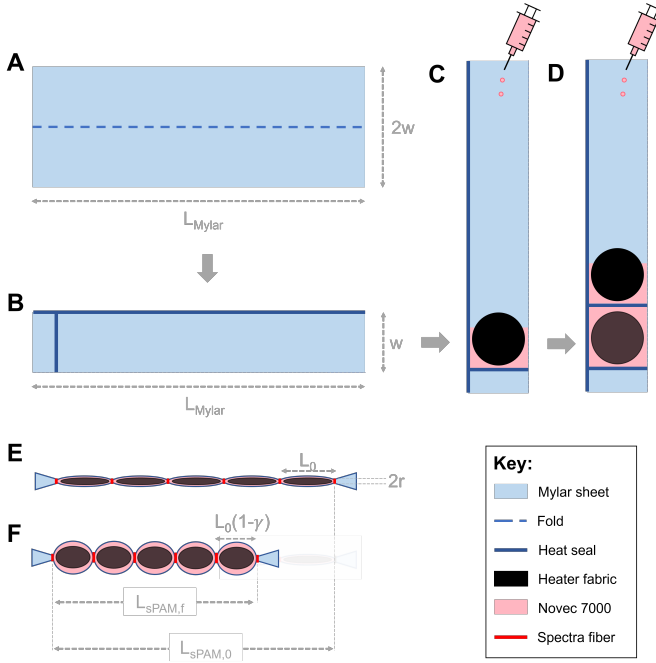


Fig. 3. Schematic of fabrication steps. **A:** Cut Mylar to size. **B:** Fold in half, length-wise, and heat-seal. **C:** Place absorber into sealed pouch; inject Novec 7000. **D:** Heat seal previous pouch; repeat for five pouches. **E:** Tie off pouches using spectra fiber. **F:** Inflated pouches show contraction.

inflation of the sPAMs. The sPAM on the heat source side experiences a significantly higher radiative flux and thus a higher temperature, and therefore inflates (i.e., contracts) more than the one on the opposing side. In addition, the inclusion of the internal absorbing sheet provides a means of “shading” the opposing-side sPAMs and the pneumatic LDPE spine offers insulation between the two—enhancing this differential effect. These design choices provide built-in feedback to the steering of the robot. As such, the robot will tend to steer towards the light source.

III. FABRICATION

The sPAMs were constructed from a 30 cm by 9 cm rectangular strip of clear Mylar folded onto itself length-wise, and heat sealed along its length. 2.5 cm from the bottom, a perpendicular heat seal creates a chamber with a width of 4.5 cm (3A, B). Next, a 3.8 cm diameter circle of heater fabric was slipped in from the unsealed edge until it reached a heat sealed edge. Thereafter, 1.5 mL of Novec 7000 was injected into the chamber, and enclosed with a heat seal 4.5 cm from the previous heat seal (3C,D). This process was repeated to produce 5 flat pouches in series. Finally, Spectra fiber (*Power Pro* 80 lb test) was tied onto the four seals separating each pouch and at the two ends (3E). Multiple sets of these 5-pouch sPAMs were then adhered to opposing sides of the pressurized LDPE spine using double-sided tape.

IV. MODELING

Modeling the robot requires coupling mechanical and heat transfer models. All processes are assumed to be quasistatic.

A. sPAM Model

To model the behavior of the sPAMs, we turned to previous modeling work on pleated pneumatic artificial muscles (PPAMs) [24], which behave similarly to an individual unit of the sPAM. For a given contraction ratio, γ , the force, F_γ , that each sPAM produces is

$$F_\gamma = \pi P_g r^2 \frac{1-2m}{2m \cos^2(\phi_r)}, \quad \frac{2r}{\cos(\phi_r)} < \frac{2w}{\pi} \quad (1)$$

P_g is the gauge pressure inside the sPAM, r is the radius of the constriction, w is the flat tubing width used for the sPAM, m and ϕ_r are parameters determined from the below system of equations.

$$\begin{cases} \frac{F(\phi_r|m)}{\sqrt{m \cos(\phi_r)}} = \frac{l}{r} \\ \frac{E(\phi_r|m)}{\sqrt{m \cos(\phi_r)}} = \frac{l}{r} \left(1 - \frac{\gamma}{2}\right) \end{cases} \quad (2)$$

F and E are the first and second incomplete elliptic integrals, respectively. The condition on the right hand side of Equation 1 is the zero parallel force condition [23], [24]. For further discussion and derivation of the force model, see [23], [24], and [25].

The gauge pressure inside the sPAM can be described by the inextensible textile model [27].

$$P_g = \begin{cases} P_{PC}(T) + \frac{n_{air}RT}{V} - P_{atm}, & P_{PC}(T) + \frac{n_{air}RT}{V} > P_{atm} \\ 0, & P_{PC}(T) + \frac{n_{air}RT}{V} \leq P_{atm} \end{cases} \quad (3)$$

$P_{PC}(T)$, T , n_{air} , R , V , P_{atm} are the Novec 7000 vapor pressure, absolute temperature, moles of residual air, ideal gas constant, sPAM volume, and atmospheric pressure, respectively. The pressure terms on the right hand side are absolute pressures. Ideally, there is no residual air inside the sPAM.

From these two models, we expect that increasing temperature increases force produced, an inverse relationship between force and contraction ratio, and a pressure independent zero force contraction ratio.

B. Heat Transfer

To fully model the heat transfer of the robot requires considering the three modes of heat transfer: conduction, convection, and radiation. Modeling the radiation exchange is particularly challenging because the radiative heat transfer is wavelength and configuration dependent. For a simple heat transfer model, we assume that each component can be modeled as a diffuse surface and that the heat transfer of each component can be described by an effective temperature, T_i . At equilibrium, the energy balance is

$$hA_i(T_i - T_\infty) = \sum_{j=1}^N A_i F_{ij}(J_j - J_i) \quad (4)$$

h represents the combined conductive and convective loss coefficient to the environment, A_i is the effective area of the component, T_i is the effective temperature, T_∞ is the effective environmental temperature, F_{ij} is the effective view factor

from element i to element j , and J is radiosity. Note that $A_i F_{ij} = A_j F_{ji}$ and $\sum F_{ij} = 1$.

Assuming the dominant heat transfer is radiative, then the best way to increase equilibrium temperature is to maximize light source absorption and minimize radiative losses (i.e., maximize $J_{\text{lightsource}} - J_i$). This can be done via selective absorption (see Section II-A).

The biggest source of uncertainty in the model is the effective view factor. As the robot deforms, the flux that each component sees is expected to change due to shielding, reflection, and re-radiation. Figure 1B shows how the robot alters the beam pattern of the light source. The best way to determine the effect of illumination on robot performance is through empirical measurements.

C. Kinematics Model

In order to determine the required steering forces and understand how temperature affects the pose of the robot, we created a simple kinematic model of the robot.

We discretize the robot into a series of N trapezoidal sections, each consisting of three springs (Figure 4). The center spring represents the pneumatic expansion force, and the two outer springs represent the sPAMs. We assume there are no forces between the trapezoidal sections, because we assume the robot is free from external contacts (i.e., on frictionless surface). We assume the torsion forces at the interfaces are minimal since the robot is locally buckled.

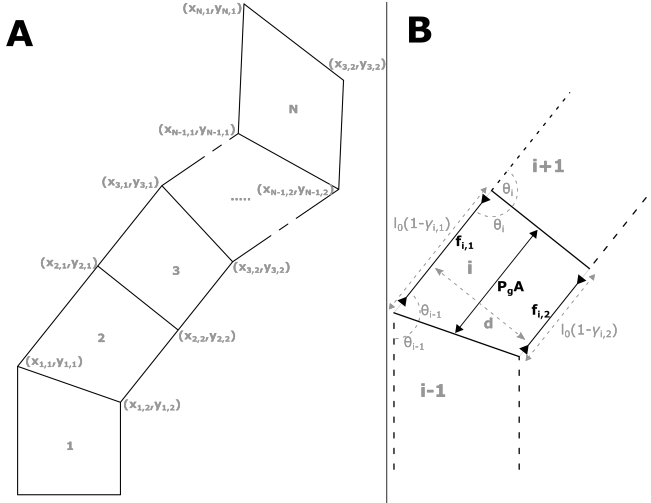


Fig. 4. **A:** Trapezoidal kinematic model. **B:** Detail of forces and key geometry.

The force and moment balances within the i -th component are

$$P_g A = f_{i,1}(\gamma_{i,1}) + f_{i,2}(\gamma_{i,2}) \quad (5)$$

$$f_{i,1}(\gamma_{i,1}) = f_{i,2}(\gamma_{i,2}) \quad (6)$$

P_g is the gauge pressure of the pneumatic backbone and A is the cross-sectional area of the backbone.

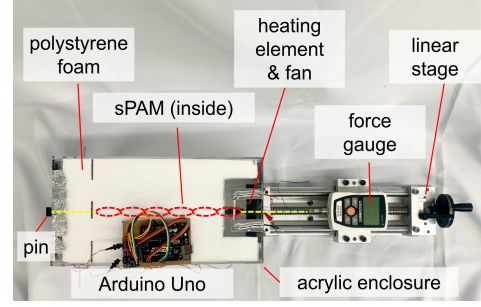


Fig. 5. Schematic showing an image the temperature-controlled experimental setup, with sPAM position indicated by red dotted lines.

This model implies that $f_{i,1}(\gamma_{i,1}) = f_{i,2}(\gamma_{i,2}) = P_g A/2$. The i -th angle can be determined from the relation

$$l_0(1 - \gamma_{i,2}) + \frac{d}{\tan(\theta_{i-1})} + \frac{d}{\tan(\theta_i)} = l_0(1 - \gamma_{i,1}) \quad (7)$$

l_0 is the free length of the section and d represents the width spacing between the two sPAMs. For simplicity, we assume this value is constant. To initialize the problem, we assume $\theta_0 = \pi/2$.

The coordinates of the points on the 1 side (e.g., heater side) of the robot are:

$$y_{i,1} = \sum_{j=1}^i \left(l_{1,j} \cos \left(\sum_{k=0}^{i-1} (\pi - 2\theta_k) \right) \right) \quad (8)$$

$$x_{i,1} = \sum_{j=1}^i \left(l_{1,j} \sin \left(\sum_{k=0}^{i-1} (\pi - 2\theta_k) \right) \right) \quad (9)$$

A similar expression can be derived for the 2 side of the robot.

This model tells us that at equilibrium the force exerted by each sPAM is independent of temperature and depends solely on the pressure of the robot's spine. However, the exact strain state (i.e., γ) requires temperature information. Interestingly, this model suggests that such a robot can be used for thermometry applications. By knowing the pose of the robot and the spine pressure, we can determine the temperatures seen by the robot, because at constant force each strain state corresponds to a unique temperature.

V. EXPERIMENTAL RESULTS

Heat transfer in radiative systems is often environmentally and configurationally dependent. To characterize the performance of our actuators, we varied the strain on the actuator and measured the corresponding force under different environmental conditions. We first tested them in a constant-temperature environment (Figure 5) before testing them in a relatively uncontrolled environment (lab space) under different illumination conditions (Figures 8,7). For each actuation test, we used sPAMs comprised of five pouches to minimize the effects of any potential manufacturing variations in a single pouch.

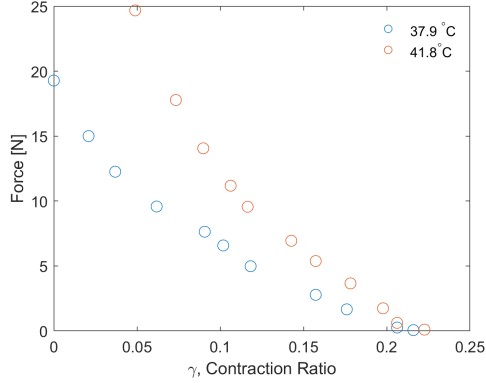


Fig. 6. Force vs. contraction ratios for different temperatures.

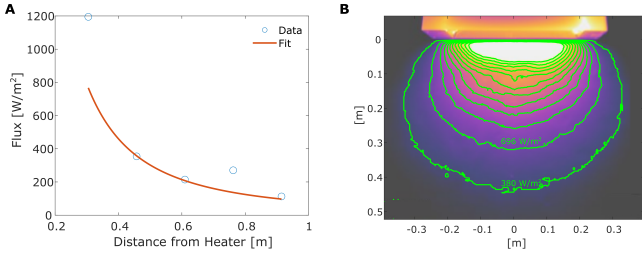


Fig. 7. **A:** Flux as a function of distance. The circles are the experimentally measured points and the solid line is an exponential fit to the data. **B:** IR image of the heat source on a polystyrene foam floor. The contours represent isotherms, which we interpret as isoflux lines.

A. Force vs. Contraction Ratio at Fixed Temperatures

For this test, a sPAM was placed in a temperature controlled box, and suspended by two pieces of Spectra fiber. One end of the fiber was pinned and the other was attached to a force gauge (Mark-10 M3-5) on a translating stage (Figure 5). To find the free length of the actuator, we translated the linear stage at room temperature ($\sim 20^\circ\text{C}$) until the sPAM transitioned from slack (0 N) to slightly tensioned (2.8 N). The contraction ratio was varied by translating the linear stage to differing positions. Figure 6 shows the force-contraction ratio relations produced by the sPAMs at two different temperatures. As predicted, force increases with temperature and varies inversely with contraction ratio, and the zero force contraction ratios are nearly the same.

B. Contraction Ratio vs. Flux at Fixed Force Level

The second set of tests measured the contraction ratio at different flux levels and a predetermined force level.

We estimated the flux experienced by the robot by measuring the equilibrium temperature, T_{plate} , of a black-painted aluminum plate ($\sim 1.6\text{ cm} \times 1.6\text{ cm}$). The center of plate was placed 2 cm above the polystyrene floor, which is approximately level with sPAMs on the robot. For simplicity, we assume the plate is a blackbody and use a vertical flat plate convection model [26] to estimate the flux as: $Q_{light} = \sigma T_{plate}^4 - h(T_{plate} - T_{amb})$. As expected, the flux roughly obeys the inverse square law. Using IR imaging (FLIR E60) we

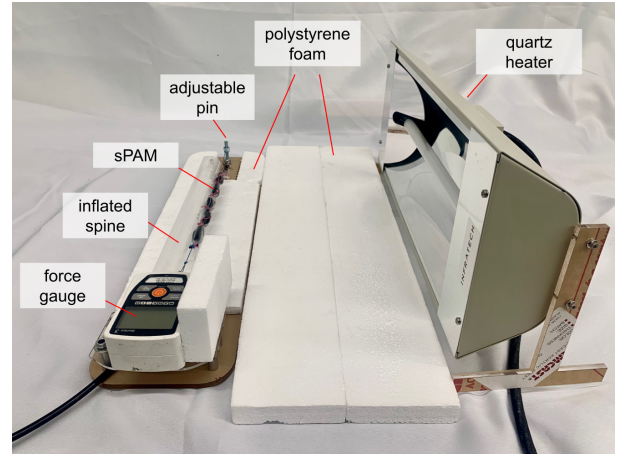


Fig. 8. Image of heat flux testing setup.

determined spatial distribution of heat around the lamp and found good agreement with the model (Figure 7).

To measure contraction ratio versus flux, we used a similar test setup as above, except now heat was provided by a quartz heater with no enclosure (Figure 8). The sPAM was backed with a 5 cm diameter LDPE tubing to simulate the heat transfer effects of the central spine. In each test, the system was equilibrated for 12 minutes to reach steady state and the screw displacement required to produce 5 N of force was measured. This allowed the contraction ratios to be measured as a function of distance and flux (Figure 9), where the flux values were derived from the fitted curve in Figure 7A.

At low flux values, the required contraction ratio varies nearly linearly with flux, then saturates at higher flux values to an upper limit that is determined by the pressure-independent zero force contraction ratio. Thus higher fluxes, which result in higher equilibrium temperatures and pressures, cannot increase contraction ratios indefinitely.

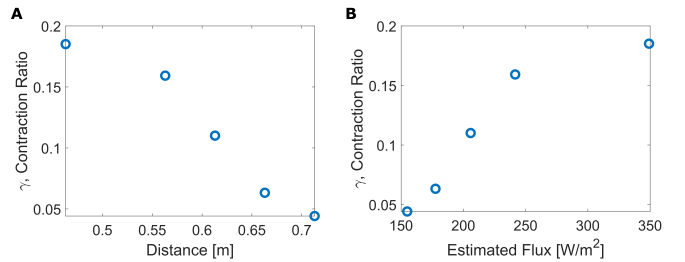


Fig. 9. Contraction ratios required to achieve 5 N of force as a function of (A) distance and (B) flux.

C. Kinematic Model Verification

We tested the kinematic model by comparing the predicted deformation of a short section of a 5-pouch robot to the experimentally-determined values (Figure 10). With respect to the center of the sPAM on the heater side, the robot was placed 55 cm away from the heater. The center body was inflated to about 12 kPa, so that the required deformation force is 5 N. To estimate the contraction ratio at this distance, we interpolated

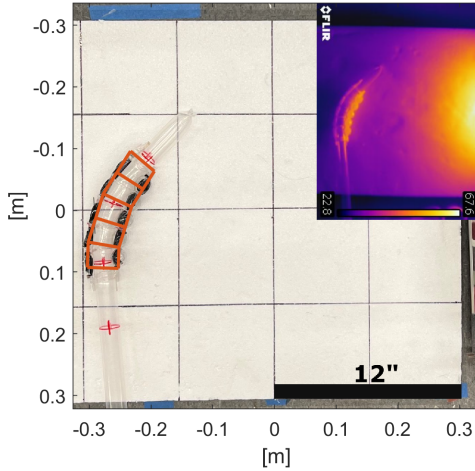


Fig. 10. Model verification on a section of robot. The predicted shape is drawn in orange. Inset shows the infrared image of a similar test setup.

the data presented in Figure 9A to find $\gamma = 0.163$. Setting $l_0 = 4.1$ cm, $d = 5.0$ cm, and $\theta_0 = \pi/2$, we computed the expected sPAM shape. When the computed shape is overlaid on the experimental image, there is good agreement, validating the utility of the model. In this approach, the sPAM positioned away from the heater is assumed to be sufficiently insulated that $\gamma = 0$, while the sPAM on the heater side is uniformly illuminated, which is consistent with infrared imaging results of a similar test (inset). We attribute the small discrepancies to unmodeled dimensional variations in the constructed sPAMs and heat transfer to the antagonistic side. It is possible that the changes in view factors and flux as the robot deforms, which are assumed to be small, also contribute to some extent.

D. Demonstration

We demonstrate the robot growing via internal pressure and steering with the heat-sensing sPAMs to find the heat source in three different scenarios. Figure 11A shows that the robot can find the heat source even if it is initially growing away from it. Figure 11B and C shows the robot navigating around simple obstacles. It is possible to increase the steering speed by placing the robot closer to the heat source (~ 35 cm), as shown in Figure 12 where ~ 90 s reorientation times are achieved. Notably, in this case, we demonstrate the turning process without eversion. Since the robot is significantly stiffer when there are sPAMs inside the spine, a higher actuation force is required, which takes longer to achieve.

VI. CONCLUSIONS AND FUTURE WORK

This work demonstrates the design, testing, modeling, and deployment of a heat-sensing vine-inspired robot capable of autonomous thermotropic motion. The robot makes use of a central pneumatically-pressurized spine for support and to drive eversion, while all sensing, control and actuation is achieved locally at a material level without central control or human intervention. We present models of the mechanical and heat transfer properties of the robot with sufficient resolution

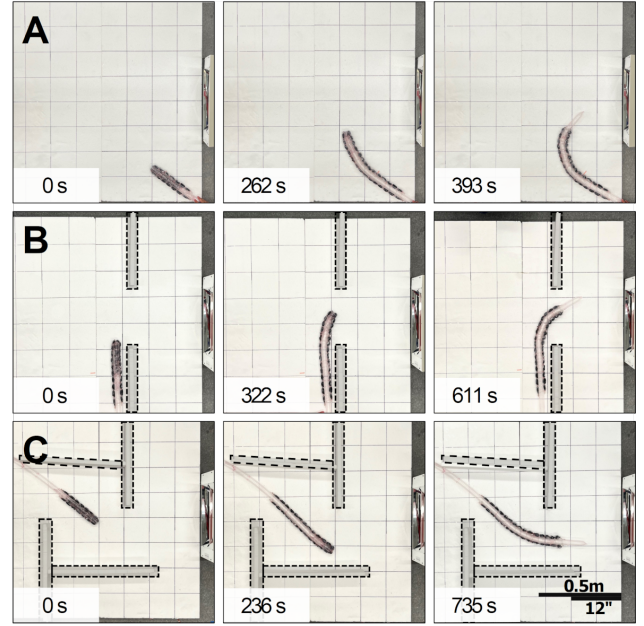


Fig. 11. Demonstrations of thermotropic eversion in unknown environments (obstacles outlined). In this timeseries, the heat source is visible at the middle right of each image. **A:** Eversion towards heater from behind. Here the vine-robot emerges from the lower right corner, with no discernable curvature along the body. As the tip grows further, the sPAMs actuate asymmetrically under thermal activation, bending and growing in a curved path toward the heat source. **B:** Eversion between two styrofoam barriers, which provide thermal shielding and define the growth path. **C:** Eversion through a simple styrofoam maze toward the heat source.

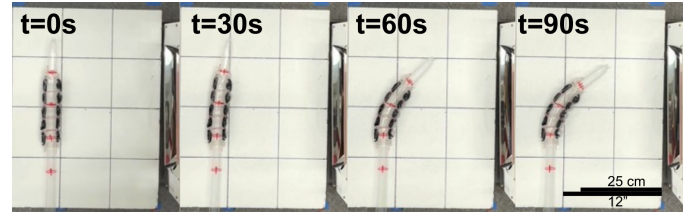


Fig. 12. The robot can steer towards the heat source within 90 s

to describe the robot's kinematic response to an external heat source. These models are validated through experimental analysis of heat-activated sPAMs, which are then incorporated into a soft robot capable of heat-sensing and thermotropic motion in unknown environments.

In the current iteration, the response of the robot is relatively slow. A heat source, such as a fire, would have much higher heat flux at equivalent or even greater distances, resulting in much faster response times. Materials with higher melting temperatures would need to be used in such cases. Another possible variation of the proposed design is to use carbon dioxide as the working fluid. Carbon dioxide absorbs strongly at the wavelengths emitted by fire, meaning the robot could selectively sense fire rather than other hot objects [28].

Overall, this demonstration represents a significant step forward in our understanding of how to incorporate material-level sensing and actuation into vine-inspired robots and soft robots generally. Future robots that build on the presented concepts could provide enhanced capabilities in search and rescue and firefighting applications.

VII. ACKNOWLEDGEMENTS

We thank Professor Michael Gordon's research group for performing the transmittance measurements in Figure 2, and David Haggerty for his editing help.

REFERENCES

- [1] E. W. Hawkes, C. Majidi, and M. T. Tolley, "Hard questions for soft robotics," *Science robotics*, vol. 6, no. 53, p. eabg6049, 2021.
- [2] D. Mishima, T. Aoki, and S. Hirose, "Development of pneumatically controlled expandable arm for search in the environment with tight access," in *Field and Service Robotics*. Springer, 2003, pp. 509–518.
- [3] T. Viebach, F. Pauker, G. Buchmann, G. Weiglhofer, and R. Pauker, "Everting sleeve system," Patent, July 5, 2006, european Patent 1676598A2.
- [4] H. Tsukagoshi, N. Arai, I. Kiryu, and A. Kitagawa, "Smooth creeping actuator by tip growth movement aiming for search and rescue operation," in *2011 IEEE International Conference on Robotics and Automation*. IEEE, 2011, pp. 1720–1725.
- [5] —, "Tip growing actuator with the hose-like structure aiming for inspection on narrow terrain," *IJAT*, vol. 5, no. 4, pp. 516–522, 2011.
- [6] A. Sadeghi, A. Tonazzini, L. Popova, and B. Mazzolai, "Robotic mechanism for soil penetration inspired by plant root," in *2013 IEEE International Conference on Robotics and Automation*. IEEE, 2013, pp. 3457–3462.
- [7] E. W. Hawkes, L. H. Blumenschein, J. D. Greer, and A. M. Okamura, "A soft robot that navigates its environment through growth," *Science Robotics*, vol. 2, no. 8, p. eaan3028, 2017.
- [8] M. M. Coad, L. H. Blumenschein, S. Cutler, J. A. R. Zepeda, N. D. Naclerio, H. El-Hussieny, U. Mehmood, J. Ryu, E. W. Hawkes, and A. M. Okamura, "Vine robots: Design, teleoperation, and deployment for navigation and exploration," in preparation.
- [9] B. Mazzolai, "Growth and tropism," *Living Machines: A Handbook of Research in Biomimetics and Biohybrid Systems*; Prescott, TJ, Lepora, N., Verschure, PFMJ, Eds, pp. 99–104, 2018.
- [10] A. Sadeghi, A. Mondini, E. Del Dottore, V. Mattoli, L. Beccai, S. Taccola, C. Lucarotti, M. Totaro, and B. Mazzolai, "A plant-inspired robot with soft differential bending capabilities," *Bioinspiration & biomimetics*, vol. 12, no. 1, p. 015001, 2016.
- [11] F. Bullo, J. Cortés, and S. Martinez, *Distributed control of robotic networks*. Princeton University Press, 2009.
- [12] B. Forde and H. Lorenzo, "The nutritional control of root development," *Plant and soil*, vol. 232, no. 1, pp. 51–68, 2001.
- [13] V. Krishnan and S. Martinez, "Distributed control for spatial self-organization of multi-agent swarms," *SIAM Journal on Control and Optimization*, vol. 56, no. 5, pp. 3642–3667, 2018.
- [14] S. Bandyopadhyay, S.-J. Chung, and F. Y. Hadaegh, "Probabilistic and distributed control of a large-scale swarm of autonomous agents," *IEEE Transactions on Robotics*, vol. 33, no. 5, pp. 1103–1123, 2017.
- [15] H. Yamaguchi, T. Arai, and G. Beni, "A distributed control scheme for multiple robotic vehicles to make group formations," *Robotics and Autonomous systems*, vol. 36, no. 4, pp. 125–147, 2001.
- [16] S. Wang, R. Zhang, D. A. Haggerty, N. D. Naclerio, and E. W. Hawkes, "A dexterous tip-extending robot with variable-length shape-locking," in *2020 IEEE International Conference on Robotics and Automation (ICRA)*. IEEE, 2020, pp. 9035–9041.
- [17] J. D. Greer, T. K. Morimoto, A. M. Okamura, and E. W. Hawkes, "A soft, steerable continuum robot that grows via tip extension," *Soft robotics*, 2018.
- [18] M. Selvaggio, L. Ramirez, N. D. Naclerio, B. Siciliano, and E. W. Hawkes, "An obstacle-interaction planning method for navigation of actuated vine robots," in *2020 IEEE International Conference on Robotics and Automation (ICRA)*. IEEE, 2020, pp. 3227–3233.
- [19] Z. Shen, F. Chen, X. Zhu, K.-T. Yong, and G. Gu, "Stimuli-responsive functional materials for soft robotics," *Journal of Materials Chemistry B*, vol. 8, no. 39, pp. 8972–8991, 2020.
- [20] Y. Zhao, M. Hua, Y. Yan, S. Wu, Y. Alsaïd, and X. He, "Stimuli-responsive polymers for soft robotics," *Annual Review of Control, Robotics, and Autonomous Systems*, vol. 5, 2021.
- [21] J. Han, W. Jiang, D. Niu, Y. Li, Y. Zhang, B. Lei, H. Liu, Y. Shi, B. Chen, L. Yin, *et al.*, "Untethered soft actuators by liquid–vapor phase transition: remote and programmable actuation," *Advanced Intelligent Systems*, vol. 1, no. 8, p. 1900109, 2019.
- [22] S. M. Mirvakili, A. Leroy, D. Sim, and E. N. Wang, "Solar-driven soft robots," *Advanced Science*, vol. 8, no. 8, p. 2004235, 2021.
- [23] J. D. Greer, T. K. Morimoto, A. M. Okamura, and E. W. Hawkes, "Series pneumatic artificial muscles (spams) and application to a soft continuum robot," in *2017 IEEE International Conference on Robotics and Automation (ICRA)*. IEEE, 2017, pp. 5503–5510.
- [24] F. Daerden and D. Lefeber, "The concept and design of pleated pneumatic artificial muscles," *International Journal of Fluid Power*, vol. 2, no. 3, pp. 41–50, 2001.
- [25] F. Daerden, "Conception and realization of pleated pneumatic artificial muscles and their use as compliant actuation elements," *Vrije Universiteit Brussel*, p. 176, 1999.
- [26] T. L. Bergman, F. P. Incropera, D. P. DeWitt, and A. S. Lavine, *Fundamentals of heat and mass transfer*. John Wiley & Sons, 2011.
- [27] V. Sanchez, C. J. Payne, D. J. Preston, J. T. Alvarez, J. C. Weaver, A. T. Atalay, M. Boyvat, D. M. Vogt, R. J. Wood, G. M. Whitesides, *et al.*, "Smart thermally actuating textiles," *Advanced Materials Technologies*, vol. 5, no. 8, p. 2000383, 2020.
- [28] R. Linares, G. Vergara, R. Gutiérrez, C. Fernández, V. Villamayor, L. Gómez, M. González-Camino, and A. Baldasano, "Gas and flame detection and identification using uncooled mwir imaging sensors," in *Thermosense: Thermal Infrared Applications XXXVII*, vol. 9485. SPIE, 2015, pp. 385–390.